# Reactive grinding synthesis of la(sr,ce)coo3 and their properties in toluene catalytic total oxidation

Bertrand Heidinger, Sebastien Royer, Jean-Marc Giraudon, Olivier Gardoll, Houshang Alamdari, Jean-Francois Lamonier

HAL Id: hal-04041327

https://hal.univ-lille.fr/hal-04041327v1

Submitted on 22 Mar 2023

# Reactive Grinding synthesis of La(Sr,Ce)CoO$_3$ and their properties in toluene catalytic total oxidation

Bertrand Heidinger,[a,b] Sébastien Royer,[a,b] Jean-Marc Giraudon,[a] Olivier Gardoll,[a] Houshang Alamdari,[b] and Jean-François Lamonier*[a,b]

**Abstract:** Perovskites-type metal oxides are an attractive alternative to noble metal-based materials for environmental catalysis. Nevertheless, they suffer from major issues such as unattractive textural properties and lower intrinsic activities than those of noble metal counterparts. Reactive grinding (RG) has been already proved to be a powerful method to produce materials with improved textural properties. La$_{1-x}$A'$_x$CoO$_3$ (A': Sr, Ce) perovskite-type materials were synthesized by RG synthesis as a 3-steps top down method: (i) conventional solid-state reaction – SSR (leading to microcrystalline material); (ii) high energy ball milling – HEBM and (iii) low energy ball milling – LEBM. The physicochemical properties of perovskite materials were investigated by XRD, N$_2$-physisorption, H$_2$-TPR, O$_2$-TPD and XPS, while their catalytic performances were evaluated for the toluene total oxidation reaction. In this study we showed that the HEBM step leads in a drastic reduction in crystal size to nanometric scale along with aggregation into dense particles. The LEBM step allows the deagglomeration of particles and specific surface areas were significantly increased. Their performances in the toluene total oxidation increased along grinding steps and a maximum of catalytic performance was observed for La$_{0.9}$Sr$_{0.1}$CoO$_3$. This material also exhibited a high catalytic stability as a function of the reaction time, under dry and wet air reaction conditions.

## Introduction

Toluene is an always widely used chemical in industrial processes. It is mainly used as an organic solvent, but also as a synthesis precursor, cleaning agent and even fuel additive. Along with benzene and xylenes, toluene forms the BTX family and counts for the major part of the industry's VOCs emissions [1] [2]. Once released in the atmosphere, toluene participates in the formation of photochemical smog and ozone by photochemical reactions [3] [4] but it can also impact human health since it has been recognized as potential CMR (Carcinogenic, Mutagenic or toxic to Reproduction), especially when mixed with benzene [5]. Long- and short-term threshold limit values (TLV) have been set up to protect workers, with respectively 20 and 100 ppm values for the European Union [6].

[a]  Univ. Lille, CNRS, Centrale Lille, ENSCL, Univ. Artois, UMR 8181 - UCCS - Unité de Catalyse et Chimie du Solide, F-59000 Lille, France
E-mail: jean-francois.lamonier@univ-lille.fr
[b]  Department of Mining, Metallurgical and Materials Engineering Université Laval, Québec, Québec G1V 0A6 (Canada)

Supporting information for this article is given via a link at the end of the document.

**Table 1.** Toluene catalytic oxidation over perovskite-type catalysts.

| Composition | conditions | WHSV GHSV | T$_{50}$ (°C) | Ref. |
|---|---|---|---|---|
| LaZn$_x$Fe$_{1-x}$O$_3$ | m$_{cat}$=200 mg 0.2 mol% tol | 15 000 h$^{-1}$ | 222-268 | [30] |
| La$_{1-x}$Sr$_x$Co$_{1-y}$Fe$_y$O$_3$ | m$_{cat}$=400 mg 500 ppmv tol | 5 700 h$^{-1}$ | 206-262 | [31] |
| La$_{1-x}$Sr$_x$CoO$_3$ | m$_{cat}$=200 mg 500 ppm tol | 30 000 L·kg$^{-1}$·h$^{-1}$ | 212-219 | [32] |
| LaMnO$_3$ | m$_{cat}$=240 mg 1000 ppm tol | 15 000 mL·g$^{-1}$·h$^{-1}$ | 193-236 | [23] |
| LaNiO$_3$ | m$_{cat}$=500 mg 500 ppm tol | 19 200 mL·g$^{-1}$·h$^{-1}$ | 224 | [33] |
| La$_{1-x}$Ca$_x$FeO$_3$ | m$_{cat}$=300 mg 4000 ppm tol | 47 000 h$^{-1}$ | 289-323 | [34] |
| La$_{1-x}$Ca$_x$NiO$_3$ | m$_{cat}$=300 mg 4000 ppm tol | 47 000 h$^{-1}$ | 297-346 | [34] |
| La$_{1-x}$Ca$_x$CoO$_3$ | m$_{cat}$=500 mg 500 ppm tol | 19 200 mL·g$^{-1}$·h$^{-1}$ | 265 | [35] |
| LaNi$_{1-y}$Co$_y$O$_{3-\delta}$ | m$_{cat}$=200 mg 500 ppm tol | 30 000 mL·g$^{-1}$·h$^{-1}$ | 218-284 | [36] |
| LaMn$_{1-x}$(Cu,Fe)$_x$O$_3$ | m$_{cat}$=200 mg 1000 ppm tol | 6000 h$^{-1}$ | 189-202 | [37] |
| La$_{0.8}$(Sr,Ce)$_{0.2}$Mn$_{0.3}$(Cu,Fe)$_{0.7}$O$_3$ | m$_{cat}$=200 mg 1000 ppm tol | 6000 h$^{-1}$ | 179-187 | [37] |
| EuCoO$_3$ | m$_{cat}$=100 mg 1700 ppm tol | 60 000 mL·g$^{-1}$·h$^{-1}$ | 256 | [38] |
| SrFeO$_{3-\delta}$ | m$_{cat}$=100 mg 1000 ppm tol | 20 000 mL·g$^{-1}$·h$^{-1}$ | 292-430 | [39] |
| SmMnO$_3$ | m$_{cat}$=100 mg 1000 ppm tol | 60 000 mL·g$^{-1}$·h$^{-1}$ | 236 | [40] |
| Eu$_{0.6}$Sr$_{0.4}$FeO$_3$ | m$_{cat}$=100 mg 1000 ppm tol | 20 000 mL·g$^{-1}$·h$^{-1}$ | 279-317 | [41] |

Perovskite-type mixed oxides of general formula of ABO$_3$ have been widely studied for several decades because of their numerous applications, especially in the field of heterogeneous

catalysis [7]. Indeed, interesting oxidative properties are reported [8] [9] while being cheaper and more available than platinoid group metals (PGM) [10], making them serious alternatives to noble metal-based catalytic formulations. With A being an alkaline, an alkaline earth or a rare-earth cation and B a transition metal, a huge number of A and B associations can be made and thus offering the possibility to finetune the perovskite properties. Among different perovskite formulations, $LaMnO_3$ and $LaCoO_3$-based perovskites often offer best catalytic performances in oxidation reactions [11-13]. In addition, perovskite structure accepts substitution of its main elements, as long as the tolerance factor $t$ is ranging between 0.75 and 1 [14], being able to form $A_{1-x}A'_xB_{1-x}B'_xO_3$ compounds. Despite B being the active site, substitution of the A site by either another rare-earth element [15] [16] or an element with a different valence such as $Sr^{2+}$ or $Ce^{4+}$ [17-19] greatly impacts the redox behavior and so the catalytic performances. This is generally explained by the change in the B site cation oxidation state and/or by the stabilization of anionic/cationic vacancies, to respect the electroneutrality of the material [20]. On the other hand, perovskite materials are very sensitive to the synthesis method [21-23], and in view of the catalytic application, it is crucial to optimize key parameters such as the specific surface area (SSA), the crystal domain size and the transition metal surface accessibility, all having important impact on the B-cation reducibility and then on the catalytic activity. Reactive Grinding (RG), as a synthesis method a commonly used in metallurgy, shows attractive features [24] [25] including a synthesis in the absence of aqueous solution step during synthesis. RG has been proved to be a sustainable and efficient synthesis method to produce catalysts such as $MnO_2$, hexaaluminates and perovskites [26-29].

In this work, nanocrystalline $La_{1-x}A'_xCoO_3$ (A': Sr, Ce) perovskite-type mixed oxides, are obtained by a three-step reactive grinding synthesis. The adopted synthesis sequence consists in: (1) a solid-state reaction step, starting from selected single oxides to obtain the perovskite phase by reaction at high temperature, (2) the structural modification (crystal size decrease) with high-energy ball milling (HEBM) step, and finally, (3) a low-energy ball milling (LEBM) for surface area development. Solids are characterized over substitution degree and catalytic performances as well as stability behavior (dry and wet conditions) are reported for the toluene total oxidation reaction.

## Results and Discussion

### *Structural properties*

X-ray diffractograms obtained for $La_{1-x}Sr_xCoO_3$ and $La_{1-x}Ce_xCoO_3$ materials are respectively shown in Figure 1 and Figure 2. $LaCoO_3$ diffractogram shows wide reflection peaks that match with those of the $LaCoO_3$ reference pattern (PDF#48-0123) with rhombohedral symmetry. The increasing of strontium results in the decrease of the full width at half maximum diffraction peaks (Figure 1). This can be explained by the change in the perovskite symmetry from rhombohedral to the cubic one ($La_{0.45}Sr_{0.55}CoO_3$, PDF#89-2528). Indeed, the disappearance of peaks at $2\theta = 33.3°$,

69.9° and the merging of others ($2\theta = 40.6°$ and 41.3°, 53.2° and 53.8°, 58.7° and 58.9° and 59.7°) are clearly observed over the SSR samples (Figure S1).
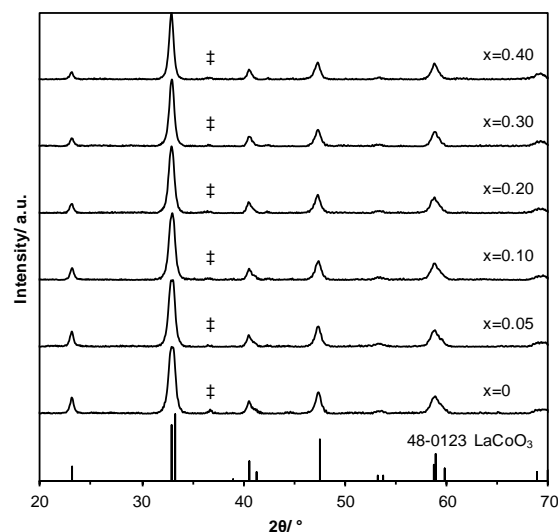


**Figure 1.** Diffractograms obtained for $La_{1-x}Sr_xCoO_3$ samples. Bottom of the figure: vertical bars are for cited JCPDS reference. ‡, $Co_3O_4$.



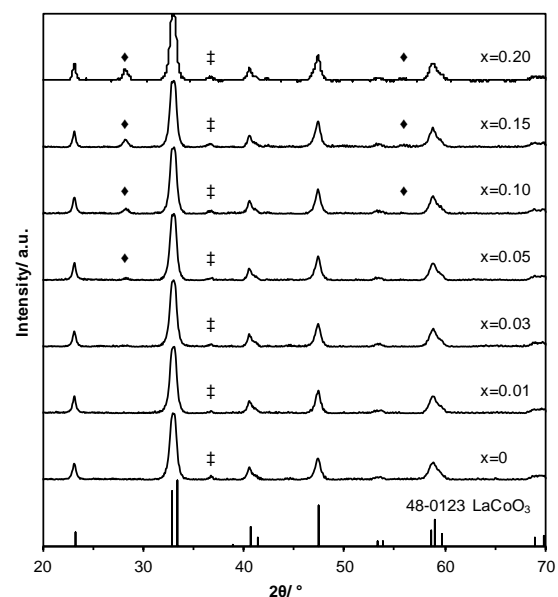**Figure 2.** Diffractograms obtained for $La_{1-x}Ce_xCoO_3$ samples. Bottom of the figure: vertical bars are for cited JCPDS reference. ‡, $Co_3O_4$; ♦, $CeO_2$.

All $La_{1-x}Ce_xCoO_3$ diffractograms exhibit diffraction peaks matching with $LaCoO_3$ (PDF#48-0123). In addition, $CeO_2$ phase (PDF#34-0394) is also detected in the samples with x>0.03 ($2\theta = 28.3°$ and 55.9°), suggesting that above this limit, cerium cannot enter anymore in the perovskite lattice and starts forming an

external secondary phase, as also reported in the literature [42]. For both $La_{1-x}Sr_xCoO_3$ and $La_{1-x}Ce_xCoO_3$, a weak reflection peak located at $2\theta = 36.7°$ is also present which can be attributed to the $Co_3O_4$ phase (PDF#42-1467). Mean crystallite sizes were estimated using the Scherrer method, taking into the account the instrumental broadening (Table 2). Calculated values are in the range of 15 to 20 nm, the unsubstituted sample having the lowest value of 15 nm. Those values are consistent with already reported perovskite synthesized by reactive grinding [27] [42] [43].

**Table 2.** Structural and textural properties obtained for $La_{1-x}A'_xCoO_3$ (A': Sr, Ce) samples.

| Sample | XRD phase | $D_{cryst}$ [a] (nm) | SSA [b] ($m^2 \cdot g^{-1}$) |
|---|---|---|---|
| LaCo | P, $Co_3O_4$ | 15 | 9 |
| LaSrCo(0.05) | P, $Co_3O_4$ | 17 | 11 |
| LaSrCo(0.10) | P, $Co_3O_4$ | 17 | 11 |
| LaSrCo(0.20) | P, $Co_3O_4$ | 17 | 12 |
| LaSrCo(0.30) | P, $Co_3O_4$ | 16 | 10 |
| LaSrCo(0.40) | P, $Co_3O_4$ | 19 | 9 |
| LaCeCo(0.01) | P, $Co_3O_4$ | 20 | 10 |
| LaCeCo(0.03) | P, $Co_3O_4$ | 19 | 10 |
| LaCeCo(0.05) | P, $Co_3O_4$, $CeO_2$ | 20 | 10 |
| LaCeCo(0.10) | P, $Co_3O_4$, $CeO_2$ | 19 | 10 |
| LaCeCo(0.15) | P, $Co_3O_4$, $CeO_2$ | 20 | 10 |
| LaCeCo(0.20) | P, $Co_3O_4$, $CeO_2$ | 20 | 10 |

P: perovskite; [a] Calculated using the Scherrer equation; [b] SSA: specific surface area.

### Surface properties

Specific surface area (SSA) values are ranging from 9 to 12 $m^2 \cdot g^{-1}$ (Table 2) without significant Sr or Ce effect on the value. A theoretical SSA of 55 $m^2 \cdot g^{-1}$ was calculated assuming a spherical-shape, a mean crystallite size of 15 nm, and a density of 7.29 $g \cdot cm^{-3}$. The gain from the low energy ball milling process is dependent of the perovskite composition and substitution is commonly found to increase specific surface area up to a certain extent [9]. The absence of change in SSA underlines the key role of the medium, ethanol instead of water, used during the LEBM process for the particle deagglomeration [27] [43] and affording a constant value of surface area whatever the perovskite composition.

X-ray photoelectron spectroscopy (XPS) has been used to probe the surface chemistry of $La_{1-x}Sr_xCoO_3$ and $La_{1-x}Ce_xCoO_3$ materials. Quantification results are shown in **Table 3**.

For $La_{1-x}Sr_xCoO_3$ samples, the A (La + Sr) and B (Co) atomic composition is in the same magnitude regardless of the x value. However, the Co atomic compositions are lower than their expected stoichiometric values. These results can be explained by the enrichment of La and Sr on the surface. Indeed, La and Sr cations can react with $H_2O$ and/or $CO_2$ to form hydroxides and/or carbonates surface species [44] [45]. XPS spectra of Co 2p core level for $LaCoO_3$ and $La_{0.6}Sr_{0.4}O_3$ samples are shown in Figure 3(A). Both samples exhibit intense Co $2p_{3/2}$ photopeaks, centered at 779.8 eV, and a satellite, shake-up peak, at higher binding energy (789.7 eV). This shape is characteristic of $Co^{3+}$ species [46] [47]. The absence of a second satellite peak at 785.9 eV (characteristic of $Co^{2+}$ species) suggests that Co is mainly in +III state. Besides the fits obtained using the pure $Co^{3+}$ species parameters from Biesinger *et al.* match well with the experimental Co $2p_{3/2}$ spectra [48]. XPS spectra of O 1s core level for $LaCoO_3$ and $La_{0.6}Sr_{0.4}O_3$ samples are shown in Figure 3(B). O 1s signal can be fitted considering three contributions: (i) low energy component (528.9 eV) assigned to lattice oxygen ($O_I$) [49], (ii) intermediate energy component (531.3 eV) attributed to surface species such as $O^-$, $O_2^-$, $HO^-$ and/or $CO_3^{2-}$ ($O_{II}$) [45] and (iii) high-energy component (533.5 eV) assigned to adsorbed $H_2O$ ($O_{III}$) [50]. For $La_{0.6}Sr_{0.4}O_3$ sample the $O_{II}$ component is predominant indicating that oxygenated surface species are more abundant in Sr substituted materials. This has already been observed by Cheng *et al.* and explained by the high reactivity of Sr cations with the environment [51]. This assumption is confirmed by the Sr 3d core level analysis (Figure 3(C)).

**Table 3.** Quantification from X-ray spectroscopy (XPS) analysis for $La_{1-x}A'_xCoO_3$ samples (A': Sr, Ce).

| Sample | La (at.%) | A' (at.%) | Co (at.%) | $\frac{Ce^{3+}}{Ce_{tot}}$ |
|---|---|---|---|---|
| LaCo | 59.0 | - | 41.0 | - |
| LaSrCo(0.05) | 54.8 | 4.9 | 40.3 | - |
| LaSrCo(0.10) | 50.3 | 7.6 | 42.0 | - |
| LaSrCo(0.20) | 43.2 | 11.8 | 45.1 | - |
| LaSrCo(0.30) | 34.9 | 18.0 | 47.1 | - |
| LaSrCo(0.40) | 29.6 | 24.3 | 46.0 | - |
| LaCeCo(0.01) | 52.8 | n.q.[a] | 47.2 | n.q. [a] |
| LaCeCo(0.03) | 52.7 | 9.5 | 37.8 | 23.2 |
| LaCeCo(0.05) | 51.4 | 12.4 | 36.3 | 25.5 |
| LaCeCo(0.10) | 44.1 | 19.3 | 36.6 | 23.8 |
| LaCeCo(0.15) | 42.8 | 24.0 | 33.2 | 18.7 |
| LaCeCo(0.20) | 36.6 | 35.4 | 27.9 | 18.8 |

[a] n.q. not quantifiable

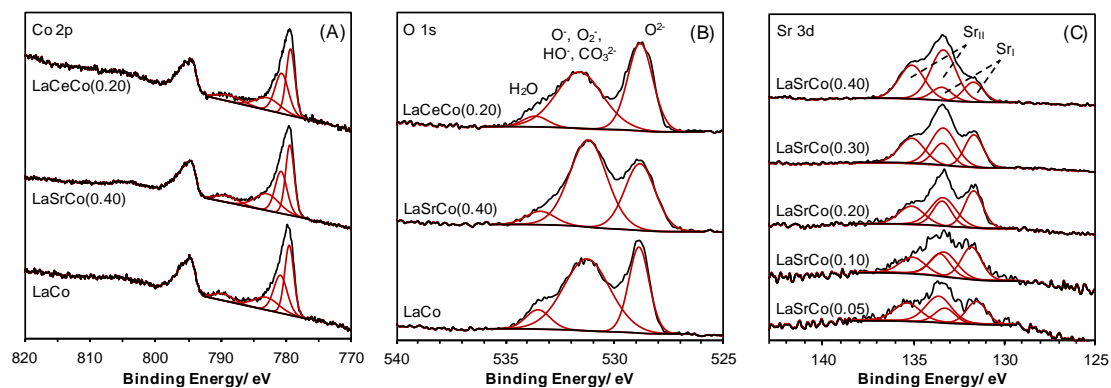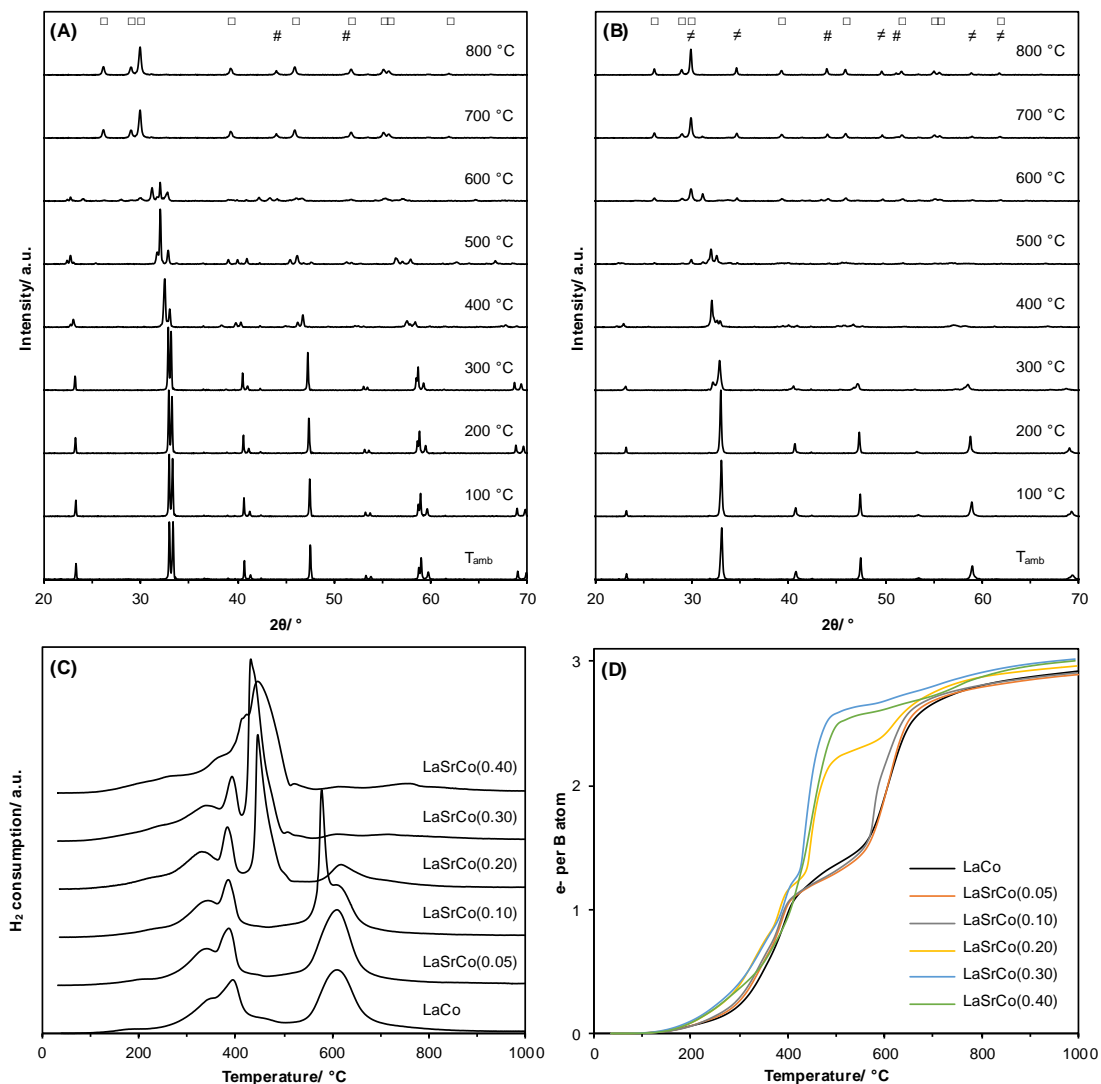**Figure 3.** High resolution spectra of (A) Co 2p, (B) O 1s and (C) Sr 3d core level spectra for $La_{1-x}Sr_xCoO_3$ and $La_{1-x}Ce_xCoO_3$ samples.



**Figure 4.** Reduction experiments for $La_{1-x}Sr_xCoO_3$ samples: High temperature x-ray diffractograms of (A) $La_{0.95}Sr_{0.05}CoO_3$ and (B) $La_{0.6}Sr_{0.4}CoO_3$, obtained from the SSR process and exposed to reductive conditions; (C) $H_2$-TPR profiles; (D) cobalt reduction degree. Symbols are: □, $La_2O_3$; #, $Co^0$; ≠, SrO.

From x = 0.05 to 0.40, the Sr 3d spectra can be reasonably fitted considering the presence of two different chemical environments for strontium sites, with a contribution from the lattice ($Sr_I$) at low binding energy (~131.6 eV) and surface strontium species ($Sr_{II}$) at higher binding energy (~133.3 eV) [51-53]. With the increasing addition of Sr, the $Sr_{II}$ component becomes predominant owing to the ease of strontium species to react with environment and to become more abundant on the surface.

For $La_{1-x}Ce_xCoO_3$ samples, the Co atomic surface compositions significantly decrease with Ce addition. This result can be explained by the presence of $CeO_2$ secondary phase, detected by XRD at low cerium content (x=0.05) (Figure 2) and probably located at the outmost surface of the perovskite particles. Co 2p and O 1s spectra are quite similar to the ones obtained for $LaCoO_3$, suggesting that (i) Co cations are in a similar chemical state ($Co^{3+}$) upon the Ce addition and that Ce cations do not resulted in a more oxygenated surface species ($O_{II}$) abundance, contrary to what had been observed with Sr cation substitution. Cerium element exhibits a 3d region with a complex photoeletronic peaks–satellites structure in addition to a mixed $Ce^{+3/+4}$ oxidation state [54] [55]. The Ce 3d signal has been fitted assuming the possibility of this mixed oxidation state, using $Ce^{+3}$ and $Ce^{+4}$ corresponding components and parameters [54]. $Ce^{3+}$ cations fraction is stable up to x=0.10, accounting for ~25% of the total cerium, to decrease for higher cerium content (Table 2). Cerium incorporation as $Ce^{4+}$ in perovskite structure should imply the decrease in Co oxidation state to *in fine* preserve the electroneutrality of the material [7]. The absence of significant modification in the Co 2p spectra previously observed, suggests that the cerium substitution mainly occurs as $Ce^{3+}$ or forms external $CeO_2$ phase. The decrease in $Ce^{3+}$ proportion at higher Ce content (x = 0.15 and 0.20) is related to the presence of $CeO_2$ segregated phase (Table 3).

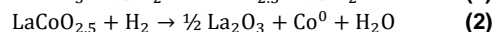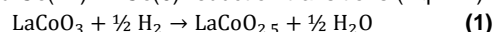### Cobalt reducibility in $La_{1-x}(Sr,Ce)_xCoO_3$

High temperature X-ray diffraction has been performed under reducing atmosphere for $La_{0.95}Sr_{0.05}CoO_3$ and $La_{0.60}Sr_{0.40}CoO_3$ samples (Figure 4(A-B)). Experiments have been conducted on the SSR samples to facilitate the phase identification. As previously described, the $La_{0.95}Sr_{0.05}CoO_3$ exhibits the $LaCoO_3$ reference phase (PDF#48-0123) at ambient temperature. No significant modification in the XRD patterns is observed below 400 °C. At this temperature, cobalt starts to be reduced into Co(II), leading to the $La_3Co_3O_8$ phase (PDF#89-1319). Brownmillerite-type $LaCoO_{2.5}$ compound (PDF# 04-008-6405) is observed at 500°C. The reduction is going on at higher temperature to give a mixture of $La_2O_3$ (2θ= 26.2°, 29.2°, 29.9°, 39.5°, 46.1°, 52.1°, 55.4°, 56.0° and 62.3°) and $Co^0$ (2θ= 44.3° and 51.7°). With a Sr content of 40 at.%, the material starts to be reduced at lower temperature in comparison with the low-content Sr counterparts. The perovskite cubic structure starts to be altered from 300°C, going through the same series of phase transitions as $La_{0.95}Sr_{0.05}CoO_3$ sample, until a total reduction of cobalt achieved at 700 °C and no more modification appears at higher temperature. In addition to $La_2O_3$ and $Co^0$ phases, SrO is also detected (PDF#06-0520, 2θ= 29.9°, 34.6°, 49.6°, 58.9° and 61.8°) when reduction temperature exceeds 500 °C.

**Table 4.** $H_2$-TPR results for $La_{1-x}Sr_xCoO_3$ and $La_{1-x}Ce_xCoO_3$ samples.

| Sample | $T_{1, max}$ (°C) | $T_{2, max}$ (°C) | $H_2$ uptake (mmol($H_2$)·$g^{-1}$) | AOS(Co) |
|---|---|---|---|---|
| LaCo | 386 | 610 | 7.04 | 2.9 |
| LaSrCo(0.05) | 386 | 610 | 7.07 | 2.9 |
| LaSrCo(0.10) | 384 | 577/608 | 7.16 | 2.9 |
| LaSrCo(0.20) | 381 | 445/617 | 7.46 | 3.0 |
| LaSrCo(0.30) | 393/432 | - | 7.77 | 3.0 |
| LaSrCo(0.40) | 446 | - | 7.90 | 3.0 |
| LaCeCo(0.01) | 398 | 609 | 6.87 | 2.9 |
| LaCeCo(0.03) | 396 | 610 | 6.96 | 2.9 |
| LaCeCo(0.05) | 397 | 606 | 7.07 | 2.9 |
| LaCeCo(0.10) | 402 | 612 | 7.09 | 2.9 |
| LaCeCo(0.15) | 400 | 609 | 7.14 | 2.9 |
| LaCeCo(0.20) | 407 | 611 | 7.25 | 2.9 |

Temperature-programmed reduction ($H_2$-TPR) profiles of $La_{1-x}Sr_xCoO_3$ and $La_{1-x}Ce_xCoO_3$ materials are shown in Figure 4 (C) and Figure 5 (A).

$H_2$-TPR profile of $LaCoO_3$ is composed of main domains: a low temperature (LT) reduction domain in the range 200–500°C, and a high temperature (HT) reduction domain in the range 500–800°C. According to the literature [15] [22], the two $H_2$ consumption events are related to the consecutive Co(+III) → Co(+II) and Co(+II) → Co(0) reduction transitions (Eq. 1-2):

$$LaCoO_3 + \frac{1}{2} H_2 \rightarrow LaCoO_{2.5} + \frac{1}{2} H_2O \qquad (1)$$
$$LaCoO_{2.5} + H_2 \rightarrow \frac{1}{2} La_2O_3 + Co^0 + H_2O \qquad (2)$$

Nonetheless, the $H_2$ uptake for the low temperature domain is superior to 1 $e^-$ per molecule of $LaCoO_3$ (Figure 4(D)) accounting for ~49% of the total consumption (Figure 4(B)). This indicates the reduction of a $Co^{3+}$ fraction up to $Co^0$ in the temperature range 200-500°C [56].

Important modifications of the $H_2$-TPR profile are observed for the Sr-substituted $LaCoO_3$ perovskites. Along Sr substitution (x < 0.4), the LT peak remains similar in shape and position. For x = 0.10, the HT peak profile is modified with the presence of an intense and narrow consumption peak at 577°C. For this composition, $H_2$ uptake ratio between the low and high temperature domains remains comparable to the $La_{0.95}Sr_{0.05}CoO_3$ and the $LaCoO_3$ ones. Increasing the strontium content from x=0.20 leads to the merging of all the reduction peaks, resulting for x=0.40 to a complex shape with a main consumption located at T= 446 °C, and two shoulders at lower temperatures (366 °C and 419 °C). The strong promotion of cobalt reduction can be related to the increase of oxygen vacancies along with Sr addition, favoring oxygen mobility, and also to changes in the Co geometry-electronic configuration [57] [58]. Indeed, XRD analysis showed the perovskite transition phase from rhombohedral to the cubic one (Figures 1 and S1).
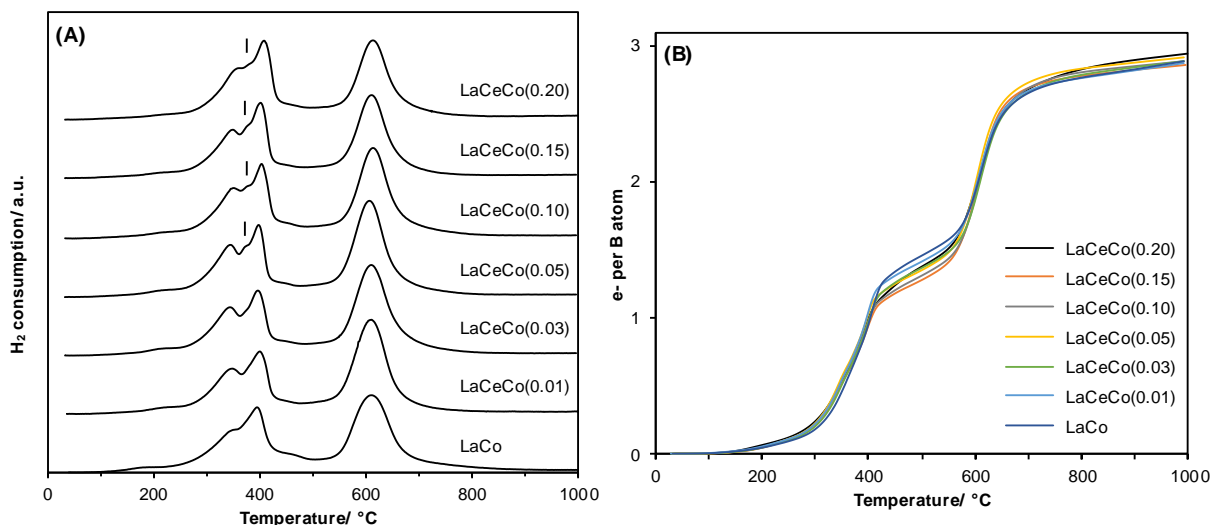
**Figure 5.** Reduction experiments for $La_{1-x}Ce_xCoO_3$ samples: (A) $H_2$-TPR profiles; (B) cobalt reduction degree.

Due to the non-reducibility of $Sr^{2+}$ (Figure 4(B)), the linear $H_2$ uptake increase with Sr content is explained by the mass difference between La and Sr atoms, making LaSrCo samples lighter and increasing Co weight concentration. In agreement with XPS analysis and whatever the x value, the Co average oxidation state was found to be 2.9-3.0 (Table 4). Therefore, the Co redox promotion by Sr is accompanied by a constant oxidation state of cobalt atoms. This result is in favor of stabilization of anion vacancies described in the literature [20] [57] [59] [60] rather than the stabilization of $Co^{4+}$, in order to ensure the chemical neutrality of the perovskite.

$H_2$-TPR profiles and cobalt reduction degree of $La_{1-x}Ce_xCoO_3$ samples are very close to the one obtained for $LaCoO_3$ perovskite (Figures 5(A-B)). It is worth noticed that above x = 0.05, a small shoulder appears at T ~ 373 °C, between the two main LT reduction peaks (Figure 5(A)). This coincides with the presence of a $CeO_2$ secondary phase identified during XRD analysis (Figure 2). Therefore, the 373 °C shoulder could be attributed to $Ce^{4+}$ reduction to $Ce^{3+}$ in external $CeO_2$ phase. Indeed, it is well known that the reduction of $CeO_2$ proceeds in two steps, the first one at low temperature (~485 °C) corresponds to the outermost surface $Ce^{4+}$ reduction while the second one at higher temperature (~750 °C) is ascribed to bulk $Ce^{4+}$ reduction [61]. The lowest temperature for surface $Ce^{4+}$ reduction and the absence of high temperature reduction peak related to bulk $Ce^{4+}$ reduction can be explained by a strong interaction between cerium and cobalt phase [62] [63] and the spillover of H atoms formed on metallic Co to the $CeO_2$ phase to promote the reduction of $Ce^{4+}$ [64]. Considering the $Ce^{4+}$ participation in the $H_2$ consumption, the Co oxidation state value is close to 3 for each $La_{1-x}Ce_xCoO_3$ samples (Table 4), in agreement with XPS results.

Oxygen temperature-programmed desorption ($O_2$-TPD) profiles of selected $La_{1-x}(Sr,Ce)_xCoO_3$ materials are shown in Figure 6.

Two kinds of oxygen species can be discerned: (i) α-oxygen, which desorbs in the 300°C – 700°C temperature range and that originates from chemisorbed oxygen bound to oxygen vacancy at the surface catalyst; (ii) β-oxygen, desorbing at higher temperature (> 700 °C), and that is ascribed to lattice oxygen desorption [22] [65].
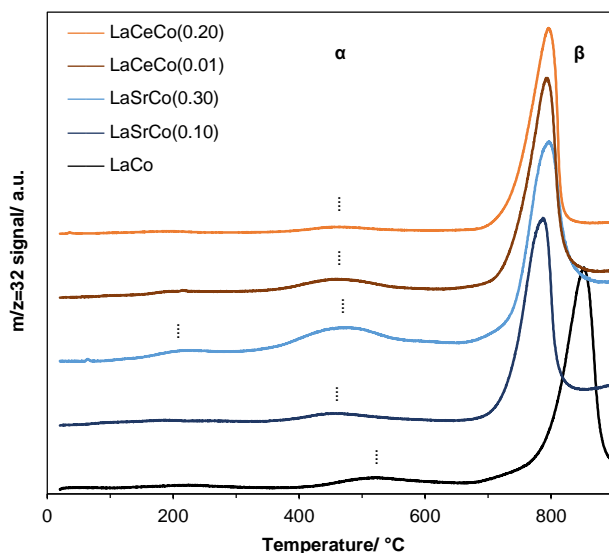


**Figure 6.** $O_2$-TPD profiles of selected $La_{1-x}(Sr,Ce)_xCoO_3$ samples (ramp = +5 °C·min$^{-1}$ under He).

All $O_2$-TPD profiles are similar, with a weak α-oxygen desorption and an intense β-oxygen desorption. When Sr is inserted in

substitution of La, the α-oxygen desorption peak shifts to the lower temperature by ~55 °C, not depending on the substitution degree. The amount of α-oxygen desorbed is 43 and 114 μmol·g$^{-1}$, respectively for LaSrCo(0.10) and LaSrCo(0.30), compared to the LaCo one (30 μmol·g$^{-1}$). It was previously demonstrated that, at iso-composition of material, α-oxygen desorption peak correlate with SSA [22]. As the analyzed samples show comparable SSA values (Table 2), the increase in the desorbed α-oxygen quantity is mainly related to the oxygen vacancy formation along with La$^{3+}$ substitution by Sr$^{2+}$ to respect the electroneutrality of the perovskite [65]. In addition to the main α-peak observed, a second low intensity desorption at lower temperature (~210°C) is observed, the LaSrCo(0.30) sample displaying the larger desorbed quantity, counting for 20 μmol·g$^{-1}$. This low temperature desorption is ascribed to oxygen atoms / dioxygen molecule weakly adsorbed to the surface [22] [65]. As observed for the α-oxygen desorption peak, β-oxygen desorption peak is shifted to the lower temperature by ~60 °C. This can be explained by the ease of oxygen to diffuse within the structure to reach the surface and desorb in the case of Sr-substituted materials, due to the formation of structural vacancies [66]. However, the amount of desorbed β-oxygen is similar for the unsubstituted and substituted perovskite (360 - 380 μmol·g$^{-1}$). In the case of Ce incorporation, comparable desorption temperature changes are observed than when Sr is incorporated, for α-peak and for β- peak. Small cerium substitution degree (LaCeCo(0.01)) leads to an increase in desorbed α-oxygen amount (60 μmol·g$^{-1}$), while a further increase in substitution value leads to a depressed quantity (21 μmol·g$^{-1}$). This depressed capacity of α-oxygen desorption can be related to the cerium segregation at the catalyst surface (in the form of CeO$_2$, Figure 2). Not notable evolution of the quantity of β-oxygen desorbed is observed with the Ce incorporation.

### *Catalysts activity*

Catalytic performances of the different perovskites were evaluated toward the toluene total oxidation reaction. Light-off curves, showing the toluene conversion into CO$_2$ as a function of temperature, are presented in Figure 7(A,C), for the Sr- and Ce-doped La$_{1-x}$(Sr,Ce)$_x$CoO$_3$ materials. No product other than CO$_2$ and H$_2$O were detected during reaction. The values of T$_{50}$ (Temperature at 50% of toluene conversion into CO$_2$) are reported in Table 5.

As shown in Figure 7(A), the addition of a small amount of strontium leads to a significant decrease in the T$_{50}$ value, the minimum being obtained for values of x = 0.1 and x = 0.2. Above x = 0.2, the T$_{50}$ increases again. Finally, for x = 0.4, the T$_{50}$ value is higher than that recorded for the LaCoO$_3$ unsubstituted catalyst.

Thus, the intrinsic activities calculated at 225°C (Table 5) for x = 0.1 and x = 0.2 are similar and the highest of the series (2.5 10$^{-5}$ mmol·s$^{-1}$·m$^{-2}$). The optimum catalytic performance observed for x = 0.1–0.2 agrees with previous results described in the literature [20] [67] (with comparable values of temperature as reported in Table 1). As previously demonstrated, all Sr-substituted materials exhibit similar average crystallite size and SSA (Table 2), but drastically different redox behaviors (Figure 4(C) and Figure 6). Sr substitution impacts perovskite crystallinity with the creation of defects and/or vacancies and a smooth transition occurs from LaCoO$_3$ to SrCoO$_{3-\delta}$, with an induced disorder maximized in between [32]. Sr-substitution tends also to promote oxygen mobility, as shown previously by O$_2$-TPD (Figure 6). From x = 0.2, a profound H$_2$-TPR profiles modification has been observed (Figure 4 (C-D)), a modification explained by a strong promotion of cobalt species reducibility. Above the value x = 0.2, the reduction of cobalt species continues to be promoted at lower temperature, while the activity in the toluene oxidation decreases, showing that a too high degree in cobalt species reduction (up to the metallic state at low temperature) could lead to their difficult reoxidation into Co$^{3+}$ by oxygen species, resulting in a decreased activity. This confirms that the Co$^{3+}$/Co$^{2+}$ redox couple is responsible for the good activity of cobalt species in VOC oxidation reactions [68-70].

The cerium substitution in LaCoO$_3$ perovskite leads to an improvement in catalytic activity for all cerium contents in the catalyst. Indeed, all the light-off curves obtained for Ce-doped LaCo catalysts are shifted towards the lowest temperatures in comparison with the one obtained in the presence of LaCoO$_3$ catalyst (Figure 7(C)). Based on the T$_{50}$ values, the best activity has been registered for the substitution value of x = 0.01 (Figure 7(C)). Beyond this concentration of cerium, the catalytic activity is decreasing and the value of T$_{50}$ increases with the cerium content up to the highest x value (inset of Figure 7(A)). However, with the increase of the Ce content, a slope disruption is observed in T$_{50}$ curve for x = 0.05. It coincides with the appearance of ceria phase in XRD (Figure 2), related to the low solubility of cerium in perovskite phase. The benefits of structural defects induced by Ce substitution [42] only impact activity of low Ce-content catalyst (x = 0.01), while the perovskite surface poisoning by CeO$_2$ for higher Ce substitution degree is probably at the origin of the depressed activity. This result is in line with O$_2$-TPD analyses, which have shown a decrease in desorbed α-oxygen for x = 0.2 in comparison with value obtained for x = 0.01. It should be noted that considering both series, LaCeCo(0.01) catalyst has a lower intrinsic activity compared to LaSrCo(0.10) and LaSrCo(0.20) samples (Table 4).
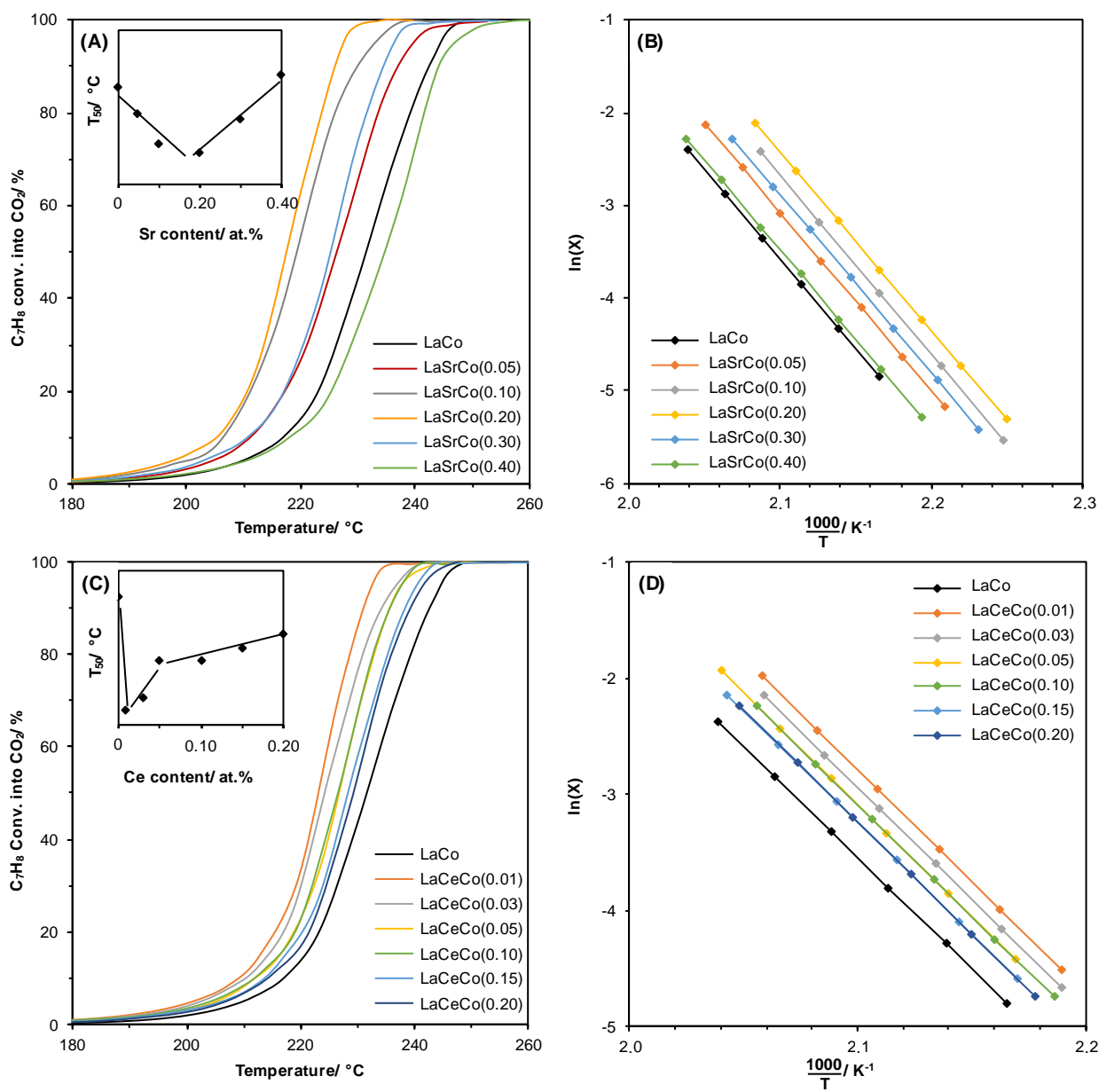
**Figure 7.** Light-off curves and corresponding corrected Arrhenius plots (X < 20%) respectively obtained for the toluene total oxidation over $La_{1-x}Sr_xCoO_3$ (A,C) and $La_{1-x}Ce_xCoO_3$ (B,D) samples. Conditions: 200 mg of catalyst, 100 mL·min$^{-1}$ of 1000 ppmv $C_7H_8$ in synthetic air (20% $O_2$ in $N_2$).
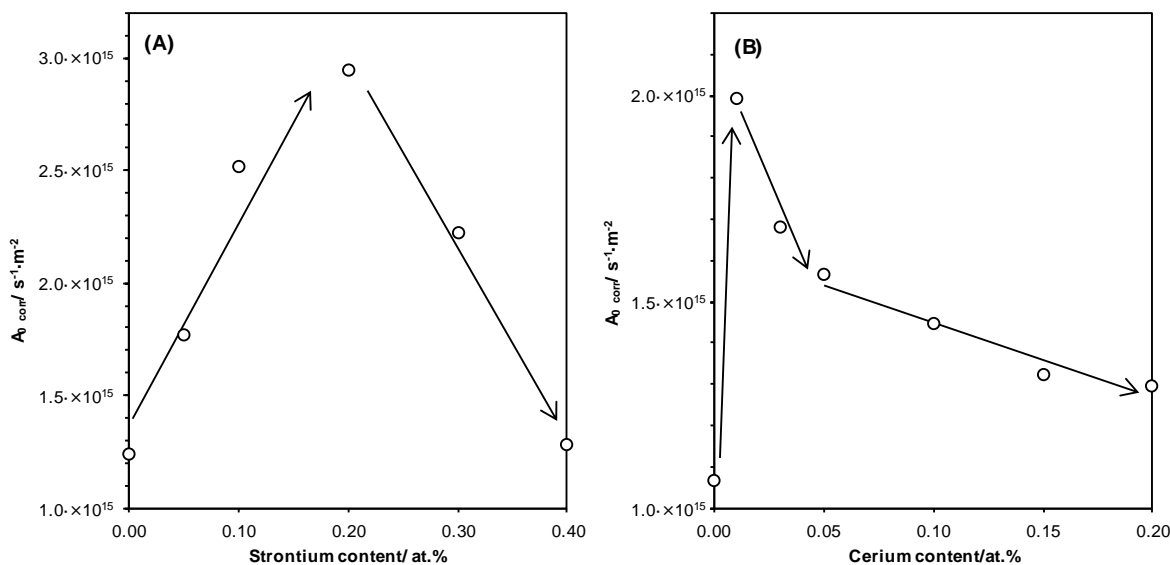
**Figure 8.** Evolution of corrected pre-exponential factor ($A_0$) with strontium (A) or Cerium (B) substitution degree.

| **Table 5.** $T_{50}$ values and kinetics data obtained from light-off curves | | | | |
|---|---|---|---|---|
| Sample | $T_{50}$ (°C) | Activity [a] (mmol·s$^{-1}$·m$^{-2}$) | Ea [b] (kJ·mol$^{-1}$) | $A_{0\ corr}$ [c] (s$^{-1}$·m$^{-2}$) |
| LaCo | 232 | $1.06 \times 10^{-5}$ | 173 | $1.2 \times 10^{15}$ |
| LaSrCo(0.05) | 226 | $1.53 \times 10^{-5}$ | 166 | $1.8 \times 10^{15}$ |
| LaSrCo(0.10) | 219 | $2.57 \times 10^{-5}$ | 162 | $2.5 \times 10^{15}$ |
| LaSrCo(0.20) | 217 | $2.43 \times 10^{-5}$ | 155 | $2.9 \times 10^{15}$ |
| LaSrCo(0.30) | 225 | $1.77 \times 10^{-5}$ | 154 | $2.2 \times 10^{15}$ |
| LaSrCo(0.40) | 235 | $7.49 \times 10^{-6}$ | 153 | $1.3 \times 10^{15}$ |
| LaCeCo(0.01) | 223 | $2.23 \times 10^{-5}$ | 157 | $2.0 \times 10^{15}$ |
| LaCeCo(0.03) | 224 | $1.90 \times 10^{-5}$ | 155 | $1.7 \times 10^{15}$ |
| LaCeCo(0.05) | 227 | $1.56 \times 10^{-5}$ | 161 | $1.6 \times 10^{15}$ |
| LaCeCo(0.10) | 227 | $1.54 \times 10^{-5}$ | 153 | $1.4 \times 10^{15}$ |
| LaCeCo(0.15) | 228 | $1.27 \times 10^{-5}$ | 165 | $1.3 \times 10^{15}$ |
| LaCeCo(0.20) | 229 | $1.17 \times 10^{-5}$ | 154 | $1.3 \times 10^{15}$ |

[a] determined at T = 225 °C; [b] determined in the range X(%) < 20%; [c] extrapolated using the Ea average value of each series and normalized with SSA.

Arrhenius plots drawn from conversion curves at X < 20% are shown in Figure 7 (B) and Figure 7 (D), assuming reaction rate of first order toward toluene concentration and of zero order toward oxygen. Activation energies (Ea), estimated from Arrhenius plot slope, and corrected pre-exponential factors ($A_{0\ corr}$) are reported in Table 5. An activation energy of 173 kJ·mol$^{-1}$ was obtained for the toluene oxidation reaction over the LaCo sample. In agreement with the Sr and Ce promotional effects, lower activation energy values are obtained for the Sr- and Ce-doped catalysts, ranging from 166 to 153 kJ·mol$^{-1}$. Theses Ea values are slightly higher than the ones observed for LaMnO$_3$ and LaFeO$_3$ systems in the exact same conditions [43] or La$_{1-x}$Ca$_x$BO$_3$ (B = Fe, Ni) systems by Pecchi *et al.* [34]. Similar to the $T_{50}$ evolution with Sr or Ce content, a curve with an optimum is observed when plotting $A_{0\ corr}$ values as a function of dopant level (Figure 8). $A_0$ is found to be maximum for the La$_{0.8}$Sr$_{0.2}$CoO$_3$ and La$_{0.8}$Ce$_{0.01}$CoO$_3$ formulations, reflecting the best activities of these two formulations per surface unit.

### Long-term stability tests

Long-term stability tests in toluene oxidation for LaCo, LaSrCo(0.10) and LaCeCo(0.01) catalysts were performed at a constant temperature of 230 °C for 70 h in similar conditions than those of the catalytic tests,. The toluene conversion into CO$_2$ is plotted as a function of the reaction time in Figure 9.

The LaCo and LaCeCo(0.01) catalysts exhibit a rapid deactivation during the first 5 hours, while the activity of LaSrCo(0.10) is quite stable for the same period. On the contrary to LaCo, the toluene conversion continues to decrease monotonously for LaCeCo(0.01) after the rapid deactivation during the first 5 hours in reaction. The deactivation resistance of the catalysts was assessed through activity coefficient a$_{230}$, evaluated by calculating the ratio of toluene conversion after 70 h of test to that obtained at the beginning of the test. Those values are quite similar for both LaCo and LaCeCo(0.01) catalysts with values of 0.77 and 0.74, respectively. This result shows that even if cerium incorporation increases the activity, it has no significant impact on the catalyst stability over long reaction time. On the contrary, LaSrCo(0.10) catalyst exhibits an excellent long-term stability in toluene oxidation. Besides the activity coefficient value a$_{230}$ for LaSrCo(0.10) is close to 1 (0.98).
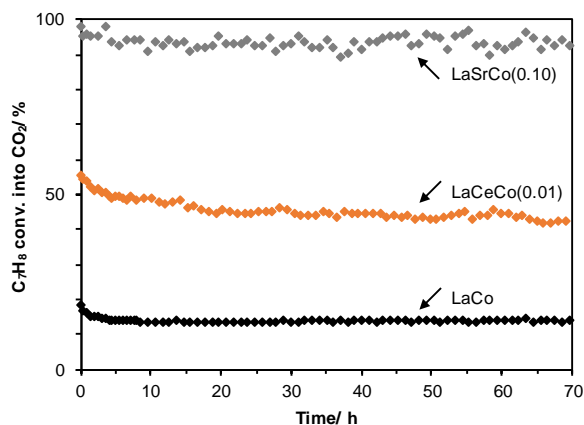
**Figure 9.** Activity stability experiments for LaCo, $La_{0.9}Sr_{0.1}CoO_3$ and $La_{0.99}Ce_{0.01}CoO_3$ samples. Conditions are: 200 mg of catalyst exposed to 1000 ppmv $C_7H_8$ in 100 mL·min$^{-1}$ of synthetic air (20% $O_2$ in $N_2$) for 70 h at a constant temperature of 230 °C.



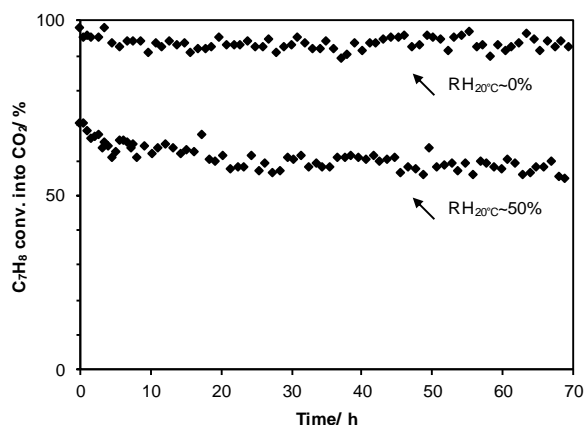**Figure 10.** Activity stability experiment for $La_{1-x}Sr_xCoO_3$ sample (x= 0.10) in wet conditions. Conditions: 200 mg of catalyst exposed to 1000 ppmv $C_7H_8$ in 100 mL·min$^{-1}$ of synthetic air (20% $O_2$ in $N_2$) for 70 h at a constant temperature of 230 °C and a relative humidity of 50% at 20°C.

In order to assess the possible application of $La(Sr,Ce)CoO_3$ catalysts for the VOC removal, it is very important to address the catalyst resistance against deactivation in the presence of water in the feed. Long-term stability of LaSrCo(0.10) catalyst was evaluated with a relative humidity at 20°C (RH$_{20°C}$) of 50% (Figure 10). The toluene conversion is lowered in the presence of water in the feed. Such behavior is frequently reported in the literature for other systems [71-75], and can be explained by a competitive adsorption between water and toluene on the active surface sites. In the presence of water, the activity coefficient value is lowered (0.83) contrary to that observed without water in the feed. However, after a rapid first step of activity stabilization of 10 h, the conversion remains quite stable during the next 60 h in reaction. It should be noted that, considering the margin of uncertainties, no SSA evolution was observed either for the used catalysts from stability tests in dry conditions or wet conditions. TPR profiles of

used LaCo and LaSrCo(0.10) samples stay unchanged (Figure S3). *A contrario*, used LaCeCo(0.01) TPR profile show small changes with the presence of two tiny hydrogen consumption peaks (red arrows, at T~ 475 °C and 725 °C) that could coincide with surface- and bulk-$CeO_2$ reduction temperature [61]. The presence of ceria related reduction peaks implies that LaCeCo is not stable over time under reaction conditions and Ce phase tends to segregate to form external surface $CeO_2$ phase. On the contrary, Sr-substituted formulation appears as a better option in view of application.

## Conclusions

$La_{1-x}Sr_xCoO_3$ and $La_{1-x}Ce_xCoO_3$ perovskites were obtained using a three-steps reactive grinding process. Synthesized catalysts showed similar textural properties (D$_{cryst}$, SSA), independent of the perovskite composition, allowing a direct and easy comparison of catalytic performances to determine the real effect of the Ce and Sr substitution on the perovskite performance. While cobalt reducibility and oxygen desorption properties were significantly modified by the strontium substitution, the cerium substitution had a much more limited impact as it segregates into an external $CeO_2$ secondary phase, when the substitution degree exceeds 0.01. The Sr-substitution modifies the structure symmetry from rhombohedral to cubic, which significantly affects Co reducibility when substitution degree exceeds 0.2. In both Ce- and Sr-substituted catalysts series, slightly lower activation energies for the toluene oxidation reaction are obtained compared to the pure perovskite. Best catalytic performances are obtained for $La_{0.9}Sr_{0.1}CoO_3$ and $La_{0.8}Sr_{0.2}CoO_3$ samples, as they are very close one to each other, followed by $La_{0.99}Ce_{0.01}CoO_3$ sample. The unsubstituted and $La_{0.99}Ce_{0.01}CoO_3$ catalysts deactivate with time, mostly in the early stages of reaction (to reach -25% after 70 h of reaction) whereas the $La_{0.9}Sr_{0.1}CoO_3$ catalyst expresses excellent stability behavior in dry air reaction condition. Adding water at a relative humidity of 50% in the reaction stream results in a loss of activity of the $La_{0.9}Sr_{0.1}CoO_3$ sample in the initial 0–10 hours period to stabilize afterwards.

## Experimental Section

*Synthesis*

Perovskite-type mixed metal oxides $La_{1-x}A'_xCoO_3$ (A' = Sr or Ce), respectively named LaCo, LaSrCo(x) and LaCeCo(x) where x represents the substitution level, were synthesized by a three-steps reactive grinding process. STEP 1 consists in a classical Solid State Reaction (SSR): oxide precursors ($La_2O_3$ and SrO or $CeO_2$ and $Co_3O_4$) were homogeneously mixed at a molar (La+A'):Co ratio equal to 1.0. Obtained powder is calcined for 4 hours at 1100 °C under static air atmosphere to obtain the perovskite phase (confirmed by XRD analysis). In STEP 2, High Energy Ball Milling (HEBM) step is performed. Milling was performed for 90 minutes using a SPEX 8000D grinder with stainless steel equipment and balls (ø 1x 11mm, 2x 12.5 mm), under static air atmosphere, at a revolution frequency of 17.5 Hz (1060 cycle.min$^{-1}$). The STEP 3 consists in the Low Energy Ball Milling

(LEBM). Milling was performed for 120 minutes using a Union Process Svegvari attritor with stainless steel equipment and balls (ø 5 mm), with addition of a small amount of ethanol (0.4 mL per g of material), and operated at a rotation speed of 450 rpm. The milled sample was recovered using 500 mL of ethanol and dried at 150 °C overnight. All materials were calcined for 3 h at 400 °C prior to characterization and catalytic performance evaluation.

*Physico-chemical characterizations*

Diffractograms were recorded on a Bruker D8 apparatus, using Cu Kα radiation ($\lambda$ = 1.54059 Å). Data were collected for $2\theta$ between 10° and 80°, with an increment of 0.05° and an integration time of 1.0 s at each step. Diffractograms were indexed using references PDF database. Crystallite mean sizes are calculated using the Scherrer equation: $D_{cryst}=(k\cdot\lambda)/(\beta\cdot cos\theta)$, where k and $\beta$ are respectively the shape factor (~0.9) and the corrected full width at half maximum of the single reflection peaks located at $2\theta$= 23.1 and 47.4°. $N_2$-physisorption experiments were collected on a Micromeritics Tristar II porosity instrument. A known mass of catalyst was degassed at 150 °C under vacuum for 6 h. Isotherms were registered at a temperature of -196 °C and SSA were determined from the adsorption branch in the 0.05-0.30 $P/P_0$ range with the Brunauer-Emmett-Teller equation (BET). Temperature-programmed reductions were performed on a Micromeritics AutoChem II 2920 chemisorption analyser. A catalyst mass, fixed to ~40 mg, was inserted in a quartz reactor and degassed under inert gas. A flow of 5 vol.% $H_2/N_2$ was stabilized at a total flow rate of 50 mL·min$^{-1}$, and the catalyst was heated from 40 °C to 1000 °C at a temperature increase rate of 10 °C·min$^{-1}$ (experimental K and P parameters respectively of 88 s and 15 °C). $O_2$-Temperature Programmed Desorption ($O_2$-TPD) experiments were carried out with the same instrument. A sample mass of ~100 mg was pretreated under synthetic air at a flow rate of 20 mL min$^{-1}$ at 400°C (temperature increase rate of 10°C min$^{-1}$) for 2 hours before being cooled to room temperature under air flow. Then the material is flushed under an inert gas flow (He, 30 mL min$^{-1}$) for 40 min. Desorption was carried out from room temperature to 1000°C under He flow (30 mL min$^{-1}$) at a heating rate of 10°C min$^{-1}$. The gas flow at the reactor outlet is analyzed using a TCD detector and a mass spectrometer (m/z= 32, $O_2$; m/z=18, $H_2O$; m/z=28, $N_2$; m/z = 44, $CO_2$). Cobalt Average oxidation state (AOS) has been calculated considering participation of $Ce^{4+}$ when appropriate (case of LaCeCo samples), which is estimated using XPS results. High temperature diffractograms are recorded on a Bruker D8 apparatus coupled to an Anton Paar XRK900 reaction cell. A known mass of catalyst, taken from the first synthesis step (*i.e.* solid-state reaction), was heated under reductive conditions (similar to TPR experiments) and data acquisition conditions are the same than XRD proceeded at ambient temperature. X-ray photoelectron spectroscopy analysis was carried out using a Kratos AXIS Ultra DLD apparatus with a monochromated Al Kα (1487 eV) source. Processing was performed using CasaXPS software, spectra being energy-corrected according to the main C 1s peak positioned at 284.8 eV. Quantification results are based on the La 3d, O 1s, Co 2p and Sr 3d or Ce 3d peak areas.

*Catalytic activity measurements*

Catalytic performances were evaluated in the gas phase toluene oxidation reaction. A mass of catalyst equal to 0.200 g was positioned in a fixed bed reactor and was heated from 25 °C to 330 °C for 30 min (2 °C·min$^{-1}$) under synthetic air flow. Then, the reaction flow, composed of 1000 ppmv of toluene diluted in synthetic air, was stabilized at a flow rate of 100 mL·min$^{-1}$ (given a WHSV = 30 000 mL·h$^{-1}$·g$^{-1}$) and the reactor temperature was allowed to decrease from 300 °C to 150 °C at a constant temperature decrease rate of -0.5 °C·min$^{-1}$. Stability experiments were performed during 70 hours at a constant temperature of 230 °C. Exhaust gases were analysed by gas chromatography and the results were expressed in terms of toluene conversion into carbon dioxide: X(%)=100·$[CO_2]_{out}$/(7·$[C_7H_8]_{in}$). Corrected pre-exponential factors ($A_{0\ corr}$) have been recalculated considering an average activation energy of 160 kJ·mol$^{-1}$ for both $La_{1-x}Sr_xCoO_3$ and $La_{1-x}Ce_xCoO_3$ samples. To quantify the resistance against deactivation an activity coefficient $a_{230}$ was defined as the ratio between the toluene conversion after 70 h reaction to that at the initial time. To mimic real conditions, catalytic performances were also evaluated in wet condition, adding water quantity to the gas stream corresponding to a relative humidity (RH) at 20 °C of 50 %.

# Acknowledgements

[1] C. He, J. Cheng, X. Zhang, M. Douthwaite, S. Pattisson, Z. Hao, *Chem. Rev.* **2019**, *119*, 4471–4568. DOI: 10.1021/acs.chemrev.8b00408

[2] Publications office of the European Union website. European Union Emission Inventory Report 1990–2015 under the UNECE Convention on Long-Range Transboundary Air Pollution (LRTAP). Available online: https://publications.europa.eu/s/kInt

[3] J.F. Hamilton, P.J. Webb, A.C. Lewis, M.M. Reviejo, *Atmos. Environ.* **2005**, *39*, 7263–7275. DOI: 10.1016/j.atmosenv.2005.09.006

[4] F. G. Shahna, F. Golbabaei, J. Hamedi, H. Mahjub, H. R. Darabi, S. J. Shahtaheri, *Chin. J. Chem. Eng.* **2010**, *18*, 113–121. DOI: 10.1016/S1004-9541(08)60331-6

[5] J.M. Donald, K. Hooper, C. Hopenhayn-Rich, *Environ. Health Perspect.* **1991**, *94*, 237–244. DOI: 10.1289/ehp.94-1567945

[6] Eur-LEX European Union Law website. Official Journal of the European Union, Commission Directive 2006/15/EC. Available online: https://eur-lex.europa.eu/eli/dir/2006/15/oj

[7] L.G. Tejuca, J.L.G. Fierro in *Properties and applications of perovskite-type oxides* (Eds.: L.G. Tejuca, J.L.G. Fierro), Marcel Dekker Inc., New York, **1993**.

[8] S. Royer, D. Duprez, *ChemCatChem* **2011**, *3*, 24–65. DOI: 10.1002/cctc.201000378]

[9] S. Royer, D. Duprez, F. Can, X. Courtois, C. Batiot-Dupeyrat, S. Laassiri, H. Alamdari, *Chem. Rev.* **2014**, *114*, 10292–10368. DOI: 10.1021/cr500032a

[10] Johnson Matthey website. PGM Market Report. Available online: http://platinum.matthey.com/

[11] J.M.D. Tascon, L.G. Tejuca, *React. Kinet. Catal. Lett.* **1980**, *15*, 185-191. DOI: 10.1007/BF02062430

[12] S. Irusta, M.P. Pina, M. Menéndez, J. Santamaría, *J. Catal.* **1998**, *179*, 400–412. DOI: 10.1006/jcat.1998.2244

[13] R. Spinicci, M. Faticanti, P. Marini, S. De Rossi, P. Porta, *J. Mol. Catal. A: Chem.* **2003**, *197*, 147–155. DOI: 10.1016/S1381-1169(02)00621-0

[14] V. M. Goldschmidt, *Die Naturwissenschaften* **1926**, *14*, 477–485. DOI: 10.1007/BF01507527

[15] M. Futai, C. Yonghua, Louhui, *React. Kinet. Catal. Lett.* **1986**, *31*, 47–53. DOI: 10.1007/BF02062510

[16] A. Baiker, P. E. Marti, P Keusch, E. Fritsch, A. Reller, *J. Cat.* **1994**, *146*, 268–276. DOI: 10.1016/0021-9517(94)90030-2

[17] N. Li, A. Boréave, J.P. Deloume, F. Gaillard, *Solid State Ion.* **2008**, *179*, 1396–1400. DOI: 10.1016/j.ssi.2008.01.060

[18] M. Schmal, CAC Perez, RNSH Magalhães, *Top Catal* **2014**, 57, 1103–1111. DOI: 10.1007/s11244-014-0275-7

[19] S. Royer, H. Alamdari, D. Duprez, S. Kaliaguine, *Appl. Catal. B Environ.* **2005**, *58*, 273–288. DOI: 10.1016/j.apcatb.2004.12.010

[20] T. Nitadori, T. Ichiki, M. Misono, *Bull. Chem. Soc. Jpn.* **1988**, *61*, 621–626. DOI: 10.1246/bcsj.61.621

[21] L. Wachowski, *Surf. Coat. Technol.* **1986**, *29*, 303–311. DOI: 10.1016/0257-8972(86)90003-4

[22] S. Royer, F. Bérubé, S. Kaliaguine, *Appl. Catal. A Gen.* **2005**, *282*, 273–284. DOI: 10.1016/j.apcata.2004.12.018

[23] C. Zhang, Y. Guo, Y. Guo, G. Lu, A. Boreave, L. Retailleau, A. Baylet, A. Giroir-Fendler, *Appl. Catal. B Environ.* **2014**, *148–149*, 490–498. DOI: 10.1016/j.apcatb.2013.11.030

[24] P. Baláž, M. Achimovičová, M. Baláž, P. Billik, Z. Cherkezova-Zheleva, J. Manuel Criado, F. Delogu, E. Dutková, E. Gaffet, F. José Gotor, R. Kumar, I. Mitov, T. Rojac, M. Senna, A. Streletskii·K. Wieczorek-Ciurowa, *Chem. Soc. Rev.* **2013**, *42*, 7571–7637. doi:10.1039/C3CS35468G

[25] H. Alamdari, S. Royer, in *Perovskites and Related Mixed Oxides* (Eds.: P. Granger, V.I. Parvulescu, S. Kaliaguine, W. Prellier), Wiley-VCH Verlag GmbH & Co. KGaA: Weinheim, Germany, **2015**; pp. 25–46. DOI: 10.1002/9783527686605

[26] C. Ciotonea, R. Averlant, G. Rochard, A. S. Mamede, J. M. Giraudon, H. Alamdari, J.-F. Lamonier, S. Royer, *ChemCatChem* **2017**, *9*, 2366-2376. DOI: 10.1002/cctc.201700199

[27] S. Laassiri, N. Bion, D. Duprez, S. Royer, H. Alamdari, *Phys. Chem. Chem. Phys.* **2014**, *16*, 4050-4060. DOI: 10.1039/C3CP54363C

[28] B. Levasseur, S. Kaliaguine, *Appl. Catal. A* **2008**, *343*, 29-38. DOI: 10.1016/j.apcata.2008.03.016

[29] Kaliaguine, S.; Van Neste, A. Process for synthesizing metal oxides and metal oxides having a perovskite or perovskite-like crystal structure. U.S. Patent 6,770,256, 3 August 2004

[30] S. A. Hosseini, M. T. Sadeghi, A. Alemi, A. Niaei, D. Salari, K. A. Leila, *Chin. J. Catal.* **2010**, *31*, 747–750. DOI: 10.1016/S1872-2067(09)60083-8

[31] S. Rousseau, S. Loridant, P. Delichere, A. Boreave, J. P. Deloume, P. Vernoux, *Appl. Catal. B Environ.* **2009**, *88*, 438–447. DOI: 10.1016/j.apcatb.2008.10.022

[32] R. Pereñiguez, J. L. Hueso, F. Gaillard, J. P. Holgado, A. Caballero, *Catal. Lett.* **2012**, *142*, 408–416. DOI: 10.1007/s10562-012-0799-z

[33] Q. Meng, W. Wang, X. Weng, Y. Liu, H. Wang, Z. Wu, *J. Phys. Chem. C* **2016**, *120*, 3259–3266. DOI: 10.1021/acs.jpcc.5b08703

[34] G. Pecchi, M.G. Jiliberto, E.J. Delgado, L.E. Cadús, J.L.G. Fierro, *J. Chem. Technol. Biotechnol.* **2011**, 86, 1067–1073. DOI: 10.1002/jctb.2611

[35] J. Zhang, D. Tan, Q. Meng, X. Wenig, Z. Wu, *Appl. Catal. B Environ.* **2015**, *172–173*, 18–26. DOI: 10.1016/j.apcatb.2015.02.006

[36] R. Pereñiguez, J. L. Hueso, J. P. Holgado, F. Gaillard, A. Caballero, *Catal. Lett.* **2009**, *131*, 164–169. DOI: 10.1007/s10562-009-9968-0

[37] A. Tarjomannejad, A. Farzi, A. Niaei, D. Salari, *Korean J. Chem. Eng.* **2016**, *33*, 2628. DOI: 10.1007/s11814-016-0108-4

[38] M. Alifanti, M. Florea, G. Filotti, V. Kuncser, V. Cortes-Corberan, V.I. Parvulescu, *Catal. Today* **2006**, *117*, 329–336. DOI: 10.1016/j.cattod.2006.05.036

[39] K. Ji, H. Dai, J. Deng, L. Zhang, F. Wang, H. Jiang, C.T. Au, *Appl. Catal. Gen.* **2012**, *425–426*, 153–160. DOI: 10.1016/j.apcata.2012.03.013

[40] L. Liu, J. Li, H. Zhang, L. Li, P. Zhou, X. Meng, M. Guo, J. Jia, T. Sun, *J. Hazard.* **2019** *362*, 178–186. DOI: 10.1016/j.jhazmat.2018.09.012

[41] K. Ji, H. Dai, J. Deng, X. Li, Y. Wang, B. Gao, G. Bai, C.T. Au, *Appl. Catal. Gen.* **2012**, *447–448*, 41–48. DOI: 10.1016/j.apcata.2012.09.004

[42] M. Ghasdi, H. Alamdari, S. Royer, A. Adnot, *Sens. Actuators B Chem.* **2011**, *156*, 147–155. DOI: 10.1016/j.snb.2011.04.003

[43] B. Heidinger, S. Royer, H. Alamdari, J.M. Giraudon, J.F. Lamonier, *Catalysts* **2019**, *9*, 633. DOI: 10.3390/catal9080633

[44] C. Zhang, C. Wang, W. Zhan, Y. Guo, Y. Guo, G. Lu, A. Baylet, A. Giroir-Fendler, *Appl. Catal. B Environ.* **2013**, *129*, 509–516. DOI: 10.1016/j.apcatb.2012.09.056

[45] J. Deng, L. Zhang, H. Dai, H. He, C. T. Au, *Ind. Eng. Chem. Res.* **2008**, *47*, 8175–8183. DOI: 10.1021/ie800585x

[46] N. S. Mc Intyre, M. G. Cook, *Anal. Chem.* **1975**, *47*, 2208–2213. DOI: 10.1021/ac60363a034

[47] J. Yang, H. Liu, W. N. Martens, R. L. Frost, *J. Phys. Chem. C* **2010**, *114*, 111–119. DOI: 10.1021/jp908548f

[48] M. C. Biesinger, B. P. Payne, A. P. Grosvenor, L. W.M. Lau, A. R. Gerson, R. St.C. Smart, *Appl. Surf. Sci.* **2011**, *257*, 2717–2730 DOI: 10.1016/j.apsusc.2010.10.051

[49] J.L.G. Fierro, L. Gonzalez Tejuca, *Appl. Surf. Sci.* **1987**, *27*, 453–457. DOI: 10.1016/0169-4332(87)90154-1

[50] J.L.G. Fierro, *Catal. Today* **1990**, *8*, 153–174. DOI: 10.1016/0920-5861(90)87016-V

[51] X. Cheng, E. Fabbri, M. Nachtegaal, I. E. Castelli, M. El Kazzi, R. Haumont, N. Marzari, T. J. Schmidt, *Chem. Mater.* **2015**, *27*, 7662–7672. doi: 10.1021/acs.chemmater.5b03138

[52] E. J. Crumlin, E. Mutoro, Z. Liu, M. E. Grass, M. D. Biegalski, Y.-L. Lee, D. Morgan, H. M. Christen, H. Bluhmg, Y. Shao-Horn, *Energy Environ. Sci.* **2012**, *5*, 6081–6088. doi: 10.1039/C2EE03397F

[53] R.P. Vasquez, *J. Electron Spectros. Relat. Phenomena* **1991**, *56*, 217–240. DOI: 10.1016/0368-2048(91)85005-E

[54] F. Le Normand, J. El Fallah, L. Hilaire, P. Légaré, A. Kotani, J.C. Parlebas, *Solid State Commun.* **1989**, *71*, 885–889. DOI: 10.1016/0038-1098(89)90555-3

[55] E. Bêche, P. Charvin, D. Perarnau, S. Abanades, G. Flamant, *Surf. Interface Anal.* **2008**, *40*, 264–267. DOI: 10.1002/sia.2686

[56] J. A. Marcos, R. H. Buitrago, E. A. Lombardo, *J. Cat.* **1987**, *105*, 95–106. DOI: 10.1016/0021-9517(87)90011-X

[57] J. L. Hueso, J. P. Holgado, R. Pereñiguez, S. Mun, M. Salmeron, A. Caballero, *J. Solid State Chem.* **2010**, *183*, 27–32. DOI: 10.1016/j.jssc.2009.10.008

[58] H Taguchi, K Matsu-ura, M Takada, K Hirota, *J. Solid State Chem.* **2012**, *190*, 157–161. DOI: 10.1016/j.jssc.2012.02.023

[59] T. Nakamura, M. Misono, Y. Yoneda, *Chem. Lett.* **1981**, *10*, 1589–1592. DOI: 10.1246/cl.1981.1589

[60] T. Nakamura, M. Misono, Y. Yoneda, *Bull. Chem. Soc. Jpn.* **1982**, *55*, 394–399. DOI: 10.1246/bcsj.55.394

[61] A. Trovarelli, *Catal. Rev.* **1996**, *38*, 439–520. DOI: 10.1080/01614949608006464

[62] L.F. Liotta, M. Ousmane, G. Di Carlo, G. Pantaleo, G. Deganello, A. Boreave, A. Giroir-Fendler, *Catal. Lett.* **2009**, *127*, 270–276. DOI: 10.1007/s10562-008-9640-0

[63] X. Xu, J. Li, Z. Hao, *J. Rare Earth* **2006**, *24*, 172–176. DOI: 10.1016/S1002-0721(06)60088-4

[64] Y. Liu, B. Liu, Q. Wang, C. Li, W. Hu, Y. Liu, P. Jing, W. Zhao, J. Zhang, *J. Catal.* **2012**, *296*, 65–76. DOI: 10.1016/j.jcat.2012.09.003

[65] J. Zhu, H. Li, L. Zhong, P. Xiao, X. Xu, X. Yang, Z. Zhao, J. Li, *ACS Catal.* **2014**, *4*, 2917-2940. DOI: 10.1021/cs500606g

[66] S. Royer, D. Duprez, S. Kaliaguine, *J. Catal.* **2005**, *234*, 364–375. DOI: 10.1016/j.jcat.2004.11.041

[67] S. Ponce, M.A. Pena, J.L.G. Fierro, *Appl. Catal. B Environ.* **2000**, *24*, 193–205. DOI: 10.1016/S0926-3373(99)00111-3

[68] F. Wyrwalski, J.-F. Lamonier, S.Siffert, A. Aboukaïs *Appl. Catal. B Environ.* **2007**, *70*, 393–399. DOI: 10.1016/j.apcatb.2006.01.023

[69] F. Wyrwalski, J.-F. Lamonier, M. J. Perez-Zurita, S. Siffert, A. Aboukaïs, *Catal. Lett.* **2006**, *108*, 87–95. DOI:10.1007/s10562-006-0018-x

[70] F. Wyrwalski, J.-F. Lamonier, S. Siffert, L. Gengembre, A. Aboukaïs, *Catal. Today* **2007**, *119*, 332–337. DOI: 10.1016/j.cattod.2006.08.025

[71] H.Y. Pan, M.Y. Xu, Z. Li, S.S. Huang, C. He, Chemosphere 2009, 76, 721–726. DOI: 10.1016/j.chemosphere.2009.04.019

[72] R. Kikuchi, S. Maeda, K. Sasaki, S. Wennerström, K. Eguchi, *Appl. Catal. Gen.* **2002**, *232*, 23–28. DOI: 10.1016/S0926-860X(02)00096-0

[73] C. Lahousse, A. Bernier, P. Grange, B. Delmon, P. Papaefthimiou, T. Ioannides, X. Verykios, *J. Catal.* **1998**, *178*, 214–225. DOI: 10.1006/jcat.1998.2148

[74] X. Li, L. Wang, Q. Xia, Z. Liu, Z. Li, *Catal. Commun.* **2011**, 14, 15–19. DOI: 10.1016/j.catcom.2011.07.003

[75] J. Hu, W. B. Li, R. F. Liu, *Catal. Today* **2018**, *314*, 147–153. DOI: 10.1016/j.cattod.2018.02.009

**Entry for the Table of Contents** (Please choose one layout)

# FULL PAPER

The effect of strontium and cerium substitution into LaCoO$_3$ materials have been studied for the toluene oxidation. Materials with better catalytic performances had been observed, due to improved redox properties. They also show very good stability with only a slight deactivation over 70 hours of reaction time.
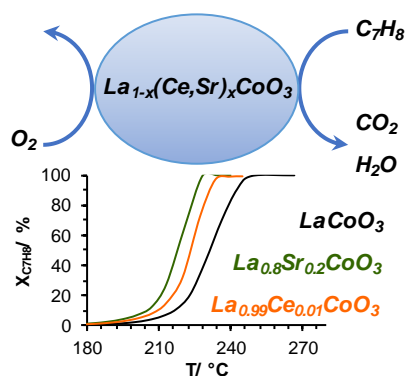
Bertrand Heidinger,[a,b] Sébastien Royer,[a,b] Jean-Marc Giraudon,[a] Olivier Gardoll,[a] Houshang Alamdari,[b] and Jean-François Lamonier*[a,b]

*Page No. – Page No.*

**Reactive Grinding synthesis of La(Sr,Ce)CoO$_3$ and their properties in toluene catalytic total oxidation**